C. CÁRDENAS
R. SUNTZ✉
J.A. DENEV
H. BOCKHORN

Two-dimensional estimation of Reynolds-fluxes and -stresses in a Jet-in-Crossflow arrangement by simultaneous 2D-LIF and PIV

Institut für Technische Chemie und Polymerchemie, Universität Karlsruhe, Kaiserstr. 12,
76131 Karlsruhe, Germany

ABSTRACT Two-dimensional maps of Reynolds-fluxes and -stresses are obtained in a Jet-in-Crossflow arrangement by measuring velocity- as well as scalar concentration-fields simultaneously. The data obtained are of special concern with respect to the development and validation of turbulence- and mixing-models. The experimental results are in good agreement with a Large Eddy Simulation of the flow configuration under investigation.

A combination of 2D-LIF- and PIV-measuring technique is applied. For PIV-measurements, droplets are added to the airflow of the crossflow and the jet, respectively. Additionally, a molecular tracer is added to the jet. The concentration distribution of this tracer is detected in the interaction zone of the jet with the crossflow by 2D-LIF. NO_2 is chosen as the tracer, because it absorbs the wavelength of the frequency doubled Nd:YAG-laser used for the PIV-measurements. Therefore, in contrast to the few simultaneous LIF-PIV-measurements known from the literature for gaseous flows, only one single double pulse laser is used for the detection of the two-dimensional concentration- and the velocity-maps.

The broadband Stokes-shifted NO_2-fluorescence signal induced by one of both Nd:YAG-double laser pulses is detected perpendicular to the propagation direction of the laser beam through an additional window in the measuring section which is also used for the detection of the Mie-scattered light. Both signals are separated from each other by a 45° dichroic mirror which transmits the fluorescence-signal whereas the Mie-scattered light is reflected perpendicular with respect to the first. The Mie-scattered light from both laser-pulses is detected by the CCD-camera of the PIV-system.

1 Introduction

The Jet-in-Crossflow arrangement (JCF) is an apparently very simple flow configuration, in which a jet is injected perpendicularly to a uniform crossflow. This flow configuration is frequently found in various industrial applications, in aviation and space flights as well as in the nature. Examples are industrial burners, RQL-gas turbines,

tube-T-mixers, plumes from chimneys, engine exhaust gas pipes, cooling towers and in flare tubes, (vertical take-off) jet aircrafts, rockets and volcanoes as well as in discharges of effluents in rivers. In this flow arrangement, the mixing process of both flows is driven by the formation of turbulent vortices, which are significantly influenced by the interaction between the jet and the crossflow. The fundamental understanding of the formation of characteristic vortex-structures and the mixing process is of special theoretical and practical relevance and consequently an objective of intense investigations over several decades [1].

These investigations show that the most important parameter describing the penetration behavior of the jet (subscript index j) into the crossflow (subscript index ∞) is characterized by the momentum-flux ratio $r = (\varrho_j U_j^2 / \varrho_\infty U_\infty^2)^{1/2}$ which simplifies for equal-density flows $\varrho_j = \varrho_\infty$ to $r = U_j / U_\infty$ [2–5]. U_j / U_∞ represents the ratio between the bulk velocity of the jet U_j and the crossflow U_∞.

The interaction between the jet and the crossflow leads to characteristic coherent vortex-structures: the counter-rotating vortex pair, the horseshoe-vortex, the wake vortices, the upright-vortices and the ring-like vortices (for details see chapter 2.2 and corresponding figures). The underlying fluid mechanical mechanisms which are responsible for the formation of these structures are extremely complex and are significantly influenced by a diversity of parameters. Therefore, the JCF-arrangement is an object of intense research activities [1, 4–8]. There is an ongoing open discussion about the mechanisms responsible for these vortex-structures which are far from being understood [3, 9–12].

In the literature the investigation of the JCF-arrangement was carried out predominantly to understand these vortex-structures and the mechanisms responsible for their formation. Surprisingly, the investigation of mixing-processes in the JCF-arrangement has taken a back seat even though the latter process is strongly influenced by these vortex-structures. It explains the surprise of Su and Mungal when they wrote in their paper [13]: "Despite the abundance of engineering applications involving molecular mixing, the body of work devoted to mixing in the cross-flowing turbulent jet is relatively small".

To understand the mechanisms which are responsible for the formation of the vortex-structures in a JCF as well as the accompanying mixing processes it is of fundamental significance to develop and validate appropriate models. This aim

✉ Fax: +49-721-608-4820, E-mail: suntz@ict.uni-karlsruhe.de

can only be achieved, if ample experimental data are available about the actual velocity- and concentration-fields – at best measured simultaneously – of the mixing fluids.

Most experimental work known from literature is restricted to the estimation of velocity fields obtained by single-point measurements using one or more hot-wire probes [2–4, 6, 9, 10, 20]. These investigations were frequently assisted by flow visualisations to acquire the global structure of the characteristic vortex-features of a JCF flow arrangement [6, 10]. The point-wise measurement of the flow field by hot-wire probes implies the disadvantage that the insertion of mechanical probes may influence the flow field under investigation. Additionally, point-wise measurements of the flow field are usually carried out in a temporal sequence which will inevitably lead to a loss of statistical information because the results obtained at the different locations in the flow are not correlated. Since the early 80's modern PIV (Particle-Image-Velocimetry) is used as a non-intrusive laser diagnostic method to estimate velocity-fields [14] which significantly stimulated the investigations carried out in the JCF. Therefore, PIV offered the possibility to quantify the vortex-structures visualized by global visualization techniques with respect to the velocity distribution [7].

In the past, concentration measurements didn't come to the fore, because – as mentioned above – one was more interested to investigate the mechanisms responsible for the formation of the vortex-structures in a JCF rather than the mixing processes. If an appropriate molecular tracer is added to the jet-flow, the mixing process in the JCF can be investigated by 2D-LIF (Laser-Induced Fluorescence) because scalar concentration-fields can be estimated [7, 15]. If PIV and 2D-LIF measurements are carried out simultaneously (simultaneous 2D-LIF-PIV), multidimensional multi-point PDFs (Probability-Density-Function) $P([C_{\text{Tracer}}]; \boldsymbol{v}; (\boldsymbol{x}_1, .., \boldsymbol{x}_n))$ can be determined spatially resolved, where $[C_{\text{Tracer}}]$ is the concentration of the tracer, $\boldsymbol{v}$ the velocity-field as a function of the two-dimensional measuring field $(\boldsymbol{x}_1, .., \boldsymbol{x}_n)$ with $\boldsymbol{x}_i = (x_i, y_i)$ or $\boldsymbol{x}_i = (x_i, z_i)$, respectively[1]. These PDFs contain the full statistical information for the mentioned physical quantities. From the PDFs the different (central) moments of the distributions, e.g. mean values and standard deviations, as well as turbulence-intensities or length-scales and in particular Reynolds-fluxes $\overline{c' v_i'}$ and -stresses $\overline{v_i' v_j'}$ can be estimated. The latter quantities reflect the enhanced fluxes of a turbulent flow compared to a laminar one.

Only very few simultaneous PIV- and 2D-LIF-measurements under reactive and non-reactive conditions are known from the literature. They were carried out e.g. by Clemens et al., Hasselbrink et al., Carter et al. and Mungal et al. [16–20]. Under non-reactive conditions acetone was chosen as a fluorescing tracer in these investigations. This tracer was excited by a XeCl-excimer-laser at 308 nm or a frequency quadrupled Nd:YAG-laser at 266 nm and the fluorescence was detected Stokes-shifted. Compared to NO_2 which is used as a tracer in this study, acetone is – from a physiological point of view – less harmful. Nevertheless, NO_2 is chosen because this tracer has (1) an absorption band at 532 nm, the wavelength of the frequency doubled Nd:YAG-laser used for PIV

and (2) the resulting Stokes-shifted fluorescence extents from 540–700 nm which can easily be detected with an intensified CCD-camera [21]. Therefore, LIF- and PIV-measurements can be carried out simultaneously by detecting the fluorescence from one of both laser pulses of the double pulse frequency doubled Nd:YAG-PIV-laser, whereas for acetone two different laser systems have to be used. The addition of NO_2 in the jet is not a significant handicap because the tracer in the jet is strongly diluted. Additionally, due to the much higher flow rate of the crossflow compared to the jet the NO_2-mole fraction is further decreased by the crossflow by a 1.5 orders of magnitude down to ~ 100 ppm.

Most et al. measured turbulent fluxes by simultaneous application of filtered Rayleigh-scattering (FRS) thermometry and PIV in a highly turbulent premixed CH_4/air flame [22, 23]. The authors used a combination of an injection-seeded, frequency-doubled single-mode Nd:YAG-laser pulse and a temporally shifted pulse of a second standard frequency doubled Nd:YAG-laser superposed upon the first one to estimate the temperature- and the velocity-field. The FRS uses the different spectral broadening of Mie- and Rayleigh-scattering originating from the TiO_2-particles used for PIV and the molecules of the gas-phase, respectively. Using the laser pulse of the narrow band laser in combination with an iodine vapour as an ultra thin notch-filter, the Mie-scattered as well as the central part of the broadened Rayleigh-scattered light is blocked whereas the remaining flanks of the latter is detected. Therefore, the temperature can be obtained from the latter Doppler broadened signal.

The work of Özcan et al. [24] and Su and Mungal [19] are examples of the few investigations known by the authors, who carried out simultaneous 2D-LIF-PIV in a JCF-arrangement to derive Reynolds-fluxes and -stresses. The investigations from Özcan et al. were carried out in a Plexiglas water channel. A fluorescent dye (Rhodamine 6G) serves as a tracer, which was added to the crossflow. The method applied in this paper offers – like the experiment of Özcan et al. – a comparatively low complexity of the experimental set-up to detect two-dimensional maps of the Reynolds-stresses and -fluxes in gaseous flows. In our gas-flow JCF-arrangement the Schmidt-number differs significantly from those in a liquid-flow set-up. Su and Mungal obtained scalar flux profiles in the center plane of their gas-phase flow arrangement by adding acetone as a fluorescing medium.

2   Experimental set-up

2.1   *The flow arrangement*

In Fig. 1 a schematic illustration of the total arrangement of the JCF is given. To derive and validate models describing the turbulent flow in the interaction zone of the jet and the crossflow and their mixing behavior the JCF-arrangement is designed to realize well defined incident flow conditions over a very wide range of Reynolds-numbers for the crossflow $700 < \text{Re}_\infty < 360\,000$ (flow rate: $3.8\,\text{m}_n^3/\text{h} < Q_\infty < 1930\,\text{m}_n^3/\text{h}$) as well as the jet $150 < \text{Re}_\text{j} < 26\,500$ ($0.05\,\text{m}_n^3/\text{h} < Q_\text{j} < 8.34\,\text{m}_n^3/\text{h}$). In the literature a "combined" Reynolds-number $\text{Re} := U_\infty D_\text{j}/\nu$ which characterizes the jet and the crossflow simultaneously is frequently used instead of $\text{Re}_\infty := U_\infty D_\infty/\nu$ and

---

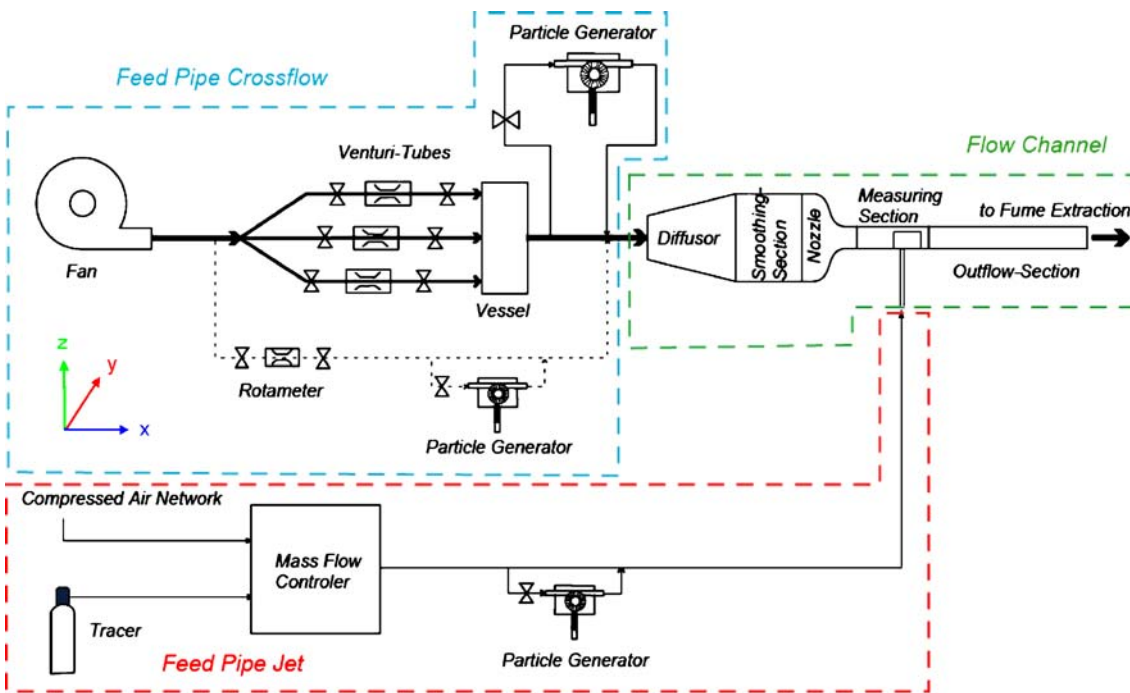[1] For definition of coordinate-system see Figs. 1 and 2.

FIGURE 1   Schematic illustration of the Jet-in-Crossflow-arrangement

$Re_j := U_j D_j / \nu$, with $D_j = 8$ mm the inner diameter of the jet, $D_\infty = 108$ mm the hydraulic diameter of the crossflow and ν the kinematic viscosity.

In the experiments the temperatures of both flows are measured to account for density variations. The effect of fluctuations of the humidity of the air is neglected, because this would influence the density of air by less than 0.5% within reasonable assumptions for these fluctuations.

In the flow arrangement a fan is used to blow ambient air into the feed pipe system of the crossflow. In order to control the air flow rate of the crossflow a rotameter or a combination of three parallel Venturi tubes is used. If low flow rates e.g. in the case of a laminar flow are chosen ($< 17.5\,\mathrm{m}_n^3/\mathrm{h}$), the rotameter is used to control the feed, whereas the Venturi tubes are preferred in the high flow rate case by successive opening of the valves in front of each Venturi tube one after each other. In the low flow rate case a vessel is used for flow homogenization in front of the real apparatus. An aerosol generator (PALAS® AGF 10.0) is used to add liquid droplets to the crossflow. These droplets serve as tracer "particles" for the PIV measurements. By using droplets instead of solid particles a static charging of the particles and a consecutive fouling of the windows for optical access in the measuring section is avoided.

After the vessel the air feed enters the diffusor in which the flow is expanded from a circular cross section of 150 mm diameter to a quadratic cross section with an edge length of 540 mm. The cone angle of the diffusor is 17° corresponding to the angle of a free jet preventing the production of additional turbulence. In the smoothing section spatial and temporal fluctuations of the feed flow is minimized by a combination of three meshes and a honey-comb structure. The latter is positioned between the first and the second mesh and serves for the elimination of swirls caused by the fan and the feed pipe sys-

tem. The meshes are used to homogenize fluctuations in the velocity of the flow over the total cross section area.

After the smoothing section a nozzle contracts the cross section area of the flow-channel from 540×540 mm to 108×108 mm which serves for a further decrease of velocity differences in the flow to form a more or less unique plug flow in the measuring section of the JCF. According to Prandtl [25] a contraction ratio not significantly lower than $k \sim 5\,(= 540\,\mathrm{mm}/108\,\mathrm{mm})$ seems to be appropriate for this purpose. Using the dimension of the contracted channel as well as the contraction ratio k, a special polynomial of 5th order described in [26] was used to estimate the contour of the nozzle. The solution of the polynomial is obtained under several constraints: among others, the total length normalized to the upstream edge length of the nozzle should be minimal, the inhomogeneity of the normalized flow velocity in the measuring section should not exceed 0.07%, and the derivative of the contour should be zero at the inlet and the outlet of the nozzle profile. The nozzle (total length: 470 mm) is made of several layers of glass fiber mats which are glued together. Acrylic varnish is used to smooth out the inner surface of the nozzle.

Downstream of the flow a stainless steel measuring section (length: 500 mm) follows the nozzle. The center of the jet (inner diameter $D_j = 8$ mm; length $= 100 \times D_j = 800$ mm) enters the measuring section 300 mm apart from the exit of the nozzle. Because the flow rate of the jet is small compared to the crossflow and NO_2 has to be added to the flow of the jet, the compressed-air system of the building in combination with a set of five appropriate mass flow controllers are used to realize the feed of the jet. The air mass flow is controlled by three mass-flow controllers (Bronkhorst Hi-Tec EL-FLOW series) of different maximum air flow rates ($100\ell_n/\mathrm{min}$, $50\ell_n/\mathrm{min}$ and $15\ell_n/\mathrm{min}$) which are arranged parallel with respect to each other. A second combination of

two parallel Bronkhorst Hi-Tec EL- air mass-flow controllers ($50\ell_n$/min and $30\ell_n$/min) is used to add the molecular tracer into the feed of the jet. By mixing the air/NO_2-mixture of a compressed gas cylinder (1.3% NO_2 in air, Air Liquide, 40l, purity 1.8, 30 bar) with the pure air flow of the jet the mole-fraction of NO_2 is decreased to $\sim$ 4000 ppm. By varying the flow rate and the number of the different parallel arranged mass flow controllers, the total flow rate of the jet as well as the NO_2-mole fraction can be adapted to the experimental re-quirements. For the PIV-measurements both flows have to be seeded with tracer-particles or droplets. Therefore, a second aerosol generator adopted to the lower flow rates of the jet compared to the crossflow (PALAS® AGK 2000) is used to add liquid droplets to the jet-flow. The size of the droplets gen-erated by both aerosol generators is $< 1\,\mu$m.

Two side windows (160×100 mm), a top window (160×72 mm) and the base-plate window (110×72 mm) serve for optical access for the laser beam and the detection system. The latter window is located between 10 mm and 120 mm be-hind the center of the jet. Although not necessarily needed for the investigations reported in this paper, synthetic quartz windows are used to allow optical access in the UV-spectral region which may be of concern in future experiments. The side windows are attached to the measuring section in such a way that optical access can be obtained at the base plate of the crossflow, where the jet enters into the crossflow.

The outflow section represents the connection between the measuring section and the exhaust system. The same stain-less steel square profile used for the measuring section serves also for the outflow section. The length of the outflow section (2500 mm) ensures that disturbances which possibly may be formed in the exhaust section of the JCF are eliminated before they propagate upstream into the measuring section.

2.2   *2D-LIF-PIV measuring system*

In Fig. 2 a schematic illustration of the 2D-LIF-PIV system is given. A frequency doubled double pulse Nd:YAG-PIV-laser (Quantel TWINS Brilliant) is used as a light source for the simultaneous LIF- as well as the PIV-measurements. The laser-pulse (135 mJ/single pulse) emitted by the laser (diameter 6 mm) is expanded into a light-sheet by means of a Galilean-telescope consisting of a cylindri-cal lens ($f_1 = -100$ mm) in combination with a spherical lens ($f_2 = 800$ mm). By this, the width of the laser beam is 48 mm and the thickness in the detection zone is $< 200\,\mu$m. In order to obtain a more or less homogeneous distribution of the laser intensity over the total detection area, the laser-light-sheet is reduced to 28 mm by an aperture. This configuration represents the best compromise between the thickness of the light-sheet and the homogeneity in the detection zone. Inves-tigations can be carried out under two different orientations of the laser beam: the laser beam propagates in the (negative) z-direction and the detection plane is the (x, z)-plane or the laser propagates in the y-direction and the detection plane is (x, y). The latter case is depicted in Fig. 2.

The signals induced in the section plane, the light scat-tered from the droplet aerosol at 532 nm as well as the broadband Stokes-shifted fluorescence from the molecu-lar tracer NO_2 (540–700 nm) are imaged perpendicular to the propagation direction of the laser beam onto ap-propriate CCD-cameras. For PIV an unintensified (Dantec 80C60 HiSense PIV/PLIF Camera, 1280×1024 pixels) and for LIF an intensified CCD-camera (Roper Scientific, PI-MAX, 512×512 pixels) are used. Both signals are separated from each other by a dichroic plate (LOT CH-Z532-90S, R_{max}@532 nm, $T_{max} = 545$–750 nm, angle of incidence: 45°),
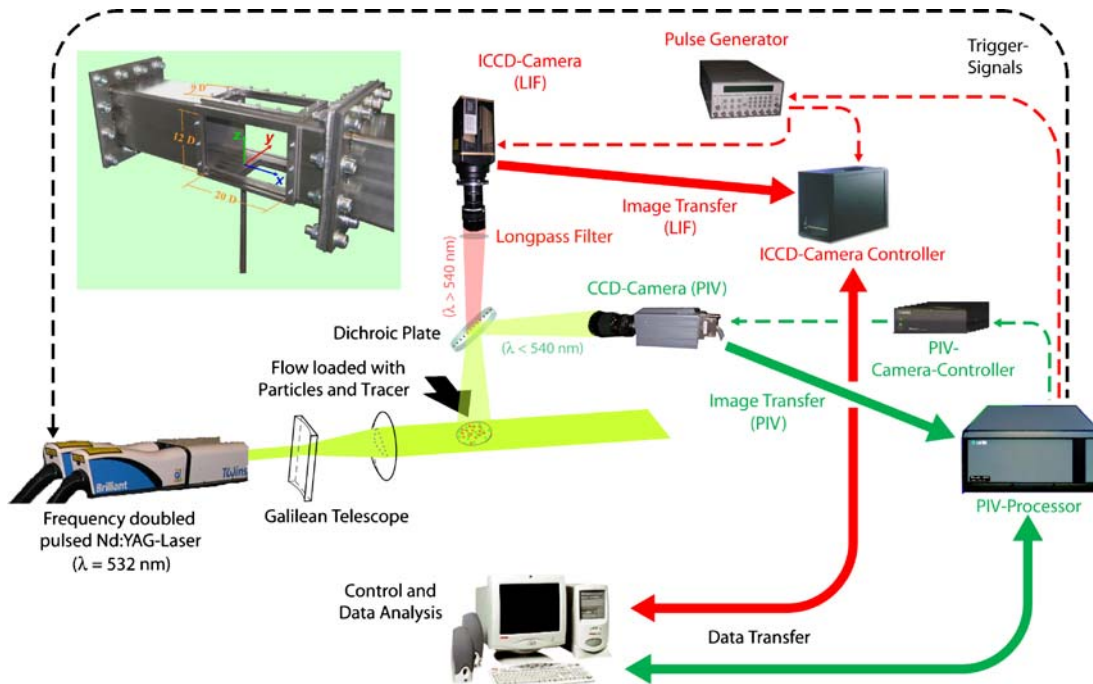
FIGURE 2   Experimental set-up of the simultaneous 2D-LIF-PIV measuring technique. In addition to the set-up the measuring section and the location of the coordinate system are given. The x-direction represents the (cross-) flow direction, y is the spanwise direction and z the vertical direction/flow direction of the jet, respectively. $D_j = 8$ mm is the inner diameter of the jet

which reflects the wavelength of the frequency doubled Nd:YAG-laser and transmits wavelengths > 532 nm. To suppress spurious scattered light from the LIF-camera, an additional dielectric coated longpass-filter (LOT CH-LP540-70S, $T_{max} = 545$–750 nm, angle of incidence: $0°$) is used in front of the ICCD-camera. These two optical elements are specially designed for our purpose, because the transmission characteristic of both, the filter and the dichroic plate, has to be adapted to the detection scheme. The wavelength of the laser should be completely suppressed in the LIF-signal whereas the edge of transmission of the filter should be very steep to get as much fluorescence-signal as possible. By using this combination of dichroic plate and longpass-filter it was guaranteed, that the scattered light was beneath the detection limit of LIF-camera.

The PIV-processor (Dantec FlowMap 1500 PIV System) serves as the master for the synchronisation of the laser and both cameras. The PIV-processor triggers the laser, the PIV-camera-controller (DANTEC HiSense-Camera-Controller) and a pulse generator (SRS DG-535). The latter serves for triggering the ICCD-camera controller (Roper Scientific ST-133) and the ICCD-camera.

For data acquisition a personal computer was used. The PIV- and the LIF-signal were analyzed with the software packet Dantec FlowManager Version 3.62 and by an own programme written in MatLab, respectively.

The LIF-signal is calibrated to absolute concentrations by measuring the fluorescence intensity in the center of the jet just upon the exit into the crossflow. At this location any dilution of the NO_2-concentration by the crossflow can be excluded. Because of the different number of pixels (LIF-camera: 512×512 pixels, PIV-camera: 1280×1024 pixels) and a different pixel dimension the image-size of both cameras has to be adapted with respect to each other. Therefore, in a first step the PIV-camera is operated with 1024×1024 pixels out of 1280×1024. In a second step, the distance to the measuring plane is varied for one camera, so that the image size is finally identical for both cameras. In order to determinate the correlation between c and v_i, 32×32 pixels of the LIF-camera are binned together by the Matlab-program to a super-pixel. The average fluorescence-signal from these 32×32 pixels is stored as the signal of this super-pixel. This procedure has been done, to correlate the LIF-signal with the interrogation-area of the PIV-camera, consisting out of 64×64 pixels. This results in an optical resolution of 1.5×1.5 mm. To increase the signal-to-noise-ratio of the PIV-measurement, a 50% overlapping for both cameras is applied – for details of PIV see e.g. [14, 27].

To estimate the NO_2 concentration- and the velocity-field of a complete plane in the JCF and taking into account an overlap of each individual frame with the adjacent frames, 15 single frames were put together. Due to the large dimension of the JCF, the apparatus cannot be displaced for measuring at different locations in the JCF. To avoid time consuming refocusing of the cameras and the adjustment of the laser-beam for different planes and positions within an individual plane, a 3D-traverse unit made from item-aluminium-profiles were assembled. Tilted mirrors for the laser, the Galilean-telescope, the dichroic-mirror and the cameras were mounted onto this unit. Within the detection volume the laser-light-sheet as well

as the cameras can be traversed with a precision of < 1 mm in the x-, y- and z-directions by three spindles.

In pre-experiments carried out with up to $10\,000$ ppm NO_2 in a flow cell, it was assured that the fluorescence-signal at constant ambient air pressure is proportional to the NO_2-concentration after excitation with a frequency doubled Nd:YAG-laser pulse. A linear relation between the NO_2-concentration and the LIF-signal was also observed by Gulati and Warren for the 488 nm emission line of an Ar^+-ion-laser [28]. These investigations were carried out up to a NO_2-mole fraction of ~ 1000 ppm.

Unfortunately, simultaneous LIF-PIV measurements are very time consuming in the system under investigation and the data generated are immense. As mentioned, each measuring plane is put together out of 15 single frames. If e.g. $n = 3000$ images at a repetition rate of 3 Hz are taken to obtain the mean values and the fluctuations of the concentration- and the velocity-fields of the flow the pure measuring time is $15 \times 3000\ 1/3\text{Hz}^{-1} = 250$ min/plane. The repetition-rate of the experiments is limited to 3 Hz by the intensified CCD-camera used for LIF and not by the repetition-rate of the laser (8 Hz). Additionally, background-subtraction of the LIF-signal and, if necessary flat-field corrections, to compensate the variations in the pixel-to-pixel sensitivity of the LIF-camera, lead to a further prolongation of the measuring time.

The processed data are 4 MB/image which results in 180 GB of disc space per plane. To account for this problem the number of repetitive measurements for a single frame n is limited in the experiments to obtain the mean value with an uncertainty of less than $\sigma_{rel,mean} := \sigma_{mean}/\phi_{mean} \leq 1\%$ (ϕ_{mean}: mean value of the velocity or the concentration). The relative standard error of the mean is given by $\sigma_{rel,mean} = \sigma_{mean}/\phi_{mean} = (\sigma/n^{1/2})/\phi_{mean} = \text{Tu}\,n^{-1/2}$, with Tu the turbulence intensity $\text{Tu} = \sigma/\phi_{mean}$ and the σ standard deviation. If the fluctuations of the flow is e.g. half as large as the mean value (Tu = 50%), than 2500 single measurements have to be done to fulfil the requirement $\sigma_{rel,mean} \leq 1\%$.

In Fig. 3 a photo of the visualized flow is given in addition to the vortex structures of a JCF. The photo has been taken by illuminating the droplets from the aerosol generator which have been added in the jet-flow by a bright lamp. The flow conditions in the photo are adjusted according to the conditions at which the experiments have been carried out: $Re_\infty = 3000$ and bulk velocity ratio $r = U_j/U_\infty = 3$.

3   Results and discussion

3.1   *Uniformity of the flow inside the JCF*

To demonstrate the uniformity of the laminar flow inside the JCF several profiles estimated by PIV are depicted in Fig. 4. The data are obtained for $Re_\infty = 2500$ without a jet-flow at $x/D_j = -2.4$ and 22 mm heights above the base plate ($z/D_j = 2.75$) of the measuring section – for measuring location see Figs. 2 and 3. The figure is obtained by averaging 200 images for this laminar flow. Due to the absence of the jet, no turbulent structures are formed by the interaction between the crossflow and the jet. Therefore, this number of images is sufficient in this case.

From the profiles one can see the uniformity of the mean velocity $\langle v_x \rangle$ in x-direction of the flow across the cross-
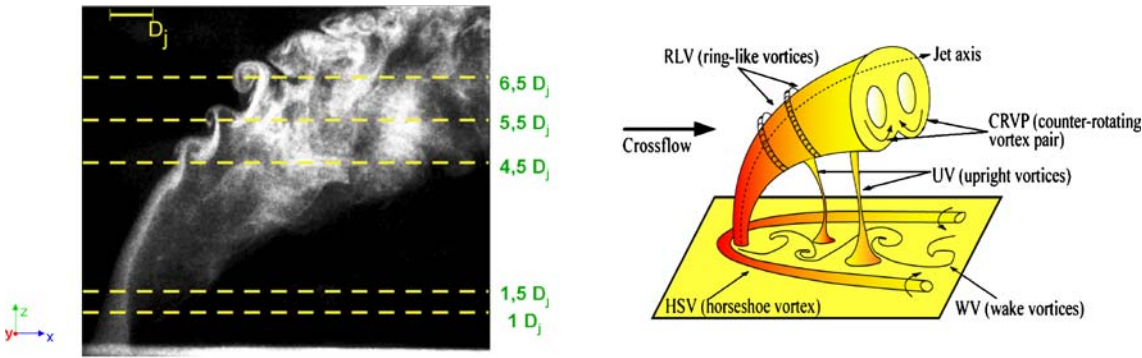
FIGURE 3 Visualization of the flow (*left figure*). Flow conditions are adjusted according to the conditions at which the experiments have been carried out: $Re_\infty = 3000$ and bulk velocity ratio $r = U_j/U_\infty = 3$. The *dotted horizontal lines* represent the measuring planes. Vortex structures of a JCF are depicted on the right figure
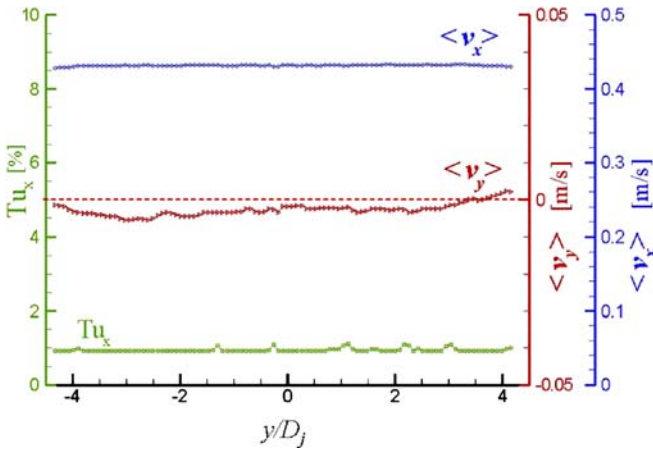
FIGURE 4 Turbulence intensity Tu_x and mean velocity-components in the x- and y-directions $\langle v_x \rangle$, $\langle v_x \rangle$ estimated by PIV. Data are obtained for $Re_\infty = 2500$ without a jet-flow at $x/D_j = -2.4$ and 22 mm heights above the base plate ($z/D_j = 2.75$) of the measuring section

section area of the JCF. The diagram additionally shows the time-averaged velocity-profile in y-direction $\langle v_y \rangle$ as well as the axial turbulence intensity Tu_x. Please note that the scales for both velocity components differ by a factor of 10. The deviation of $\langle v_y \rangle$ and Tu_x from zero reflects the non-perfectness of the axial laminar flow, respectively. Nevertheless, the fluctuations of the flow in axial direction as well as the maximum value of $\langle v_y \rangle/\langle v_x \rangle$ across the y-axis are smaller than 1%.

3.2 Concentration and velocity measurements

In Fig. 5 the maps of the measured (left row) as well as the numerically simulated (right row) normalized averaged NO_2-concentrations $\langle c \rangle$, normalized mean axial velocities $\langle v_x \rangle/U_{max}$ and axial turbulence intensities $Tu_x = \sigma(v_x)/\langle v_x \rangle$ are depicted at $z/D_j = 1.5$ (Fig. 5a) and $z/D_j = 5.5$ (Fig. 5b). U_{max} is the maximum axial velocity over the total cross-section area of the flow and $c = C/C_{jet}$ the normalized NO_2-concentration, where C is the local NO_2-concentration and C_{jet} the pure jet NO_2-concentration in mol/l, respectively. Flow conditions of the JCF are $Re_\infty = 3000$ and bulk velocity ratio $r = U_j/U_\infty = 3$. The maps are obtained from the average of 200 single images

depicted in Fig. 5a and 900, due to the higher degree of turbulence, in Fig. 5b.

In addition to the results of the measurements depicted in Fig. 5, the corresponding quantities are numerically calculated by LES (Large-Eddy-Simulation) for the same flow-conditions. The computations utilize the dynamic Smagorinsky subgrid-scale model and the gradient diffusion hypothesis for the turbulent scalar fluxes on a curvilinear numerical grid with 6.7 Mio control volumes, for more numerical details see e.g. [29]. All statistical quantities have been obtained after averaging over 90 dimensionless time units D_j/U_∞.

At $z/D_j = 1.5$ the normalized NO_2-concentration maps obtained from the LIF-measurements reveal the most characteristic flow feature of a JCF, the counter-rotating vortex pair, because the jet penetrates perpendicular into the measuring plane (see also Fig. 3). At higher heights above the base plate the jet is bent by the crossflow towards the horizontal direction. As a consequence, this flow feature cannot be easily recognized by measuring planes which are orientated parallel to the base plate. Therefore, the normalized concentration map is omitted in the figure at $z/D_j = 5.5$.

The cross section area of the structures visualized in the images at $z/D_j = 1.5$ is somewhat higher for experimental results compared to the numerical calculations. Additionally, the turbulence intensity at $z/D_j = 5.5$ is greater in the experiments compared to the simulation (please note the scaling factor 2 for the numerical simulation in the figure). This difference may be explained by small deviations in the bulk velocity ratio r. Inaccuracies in the estimation of the z-position of the plane under investigation between the experiments and the numerical simulation may be also responsible for this effect. Nevertheless, the agreement between the numerical simulation and the experimental result with respect to the location of the structures as well as the magnitude of the measured quantities is quite promising.

### 3.3 Estimation of Reynolds-fluxes and -stresses

In Fig. 6a the two-dimensional maps of the measured variances $\langle c'c' \rangle := \overline{c'^2}$ (top) of the normalized NO_2-concentration, the normalized Reynolds-fluxes $\langle v'_y c' \rangle/U_{max}$ (in the middle) and $\langle v'_x c' \rangle/U_{max}$ (bottom) are given for various (xy)-planes. In Fig. 6b the Reynolds-stresses $\langle v'_y v'_y \rangle/U_{max}^2$ (top), $\langle v'_x v'_x \rangle/U_{max}^2$ (in the middle) and $\langle v'_x v'_y \rangle/U_{max}^2$ (bot-
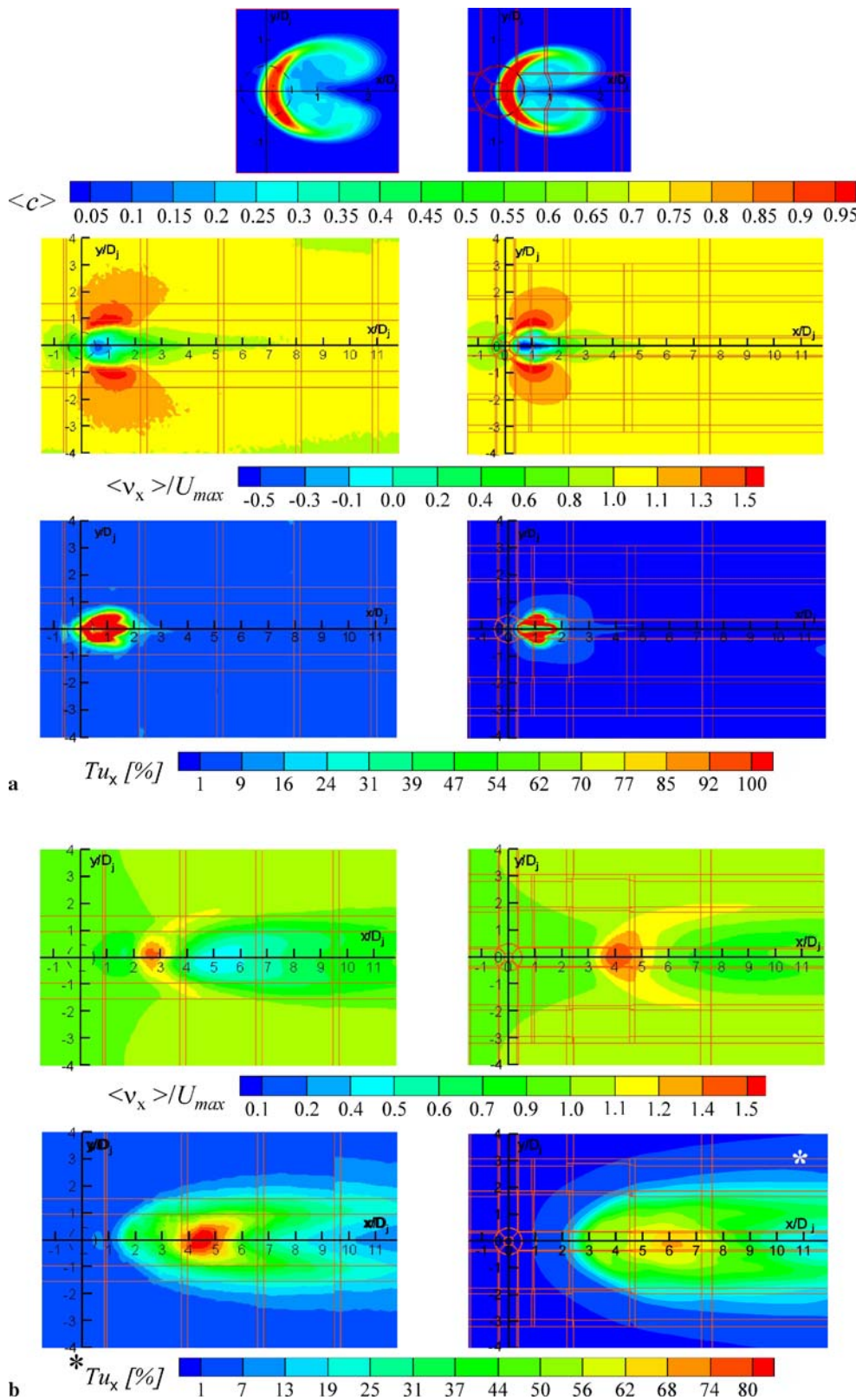
FIGURE 5 Two-dimensional maps of measured (*left column*) and numerically simulated (*right column*) normalized averaged NO_2-concentrations $\langle c \rangle$, normalized mean axial velocities $\langle v_x \rangle / U_{max}$ and axial turbulence intensities $Tu_x = \sigma(v_x)/\langle v_x \rangle$ at $z/D_j = 1.5$ (Fig. 5a) and $z/D_j = 5.5$ (Fig. 5b). In the frame indicated by (*) Tu_x is multiplied by a factor of 2. U_{max} is the maximum axial velocity over the total cross-section area of the flow and $c = C/C_{jet}$, with C the local NO_2-concentration and C_{jet} the pure jet NO_2-concentration in mol/l, respectively. Flow parameters of the JCF are $Re_\infty = 3000$ and bulk velocity ratio $r = U_j/U_\infty = 3$

tom) are depicted, additionally. The left column represents the (xy)-plane at $z/D_j = 4.5$, the column in the middle the (xy)-plane at $z/D_j = 5.5$ and the right column the (xy)-plane at $z/D_j = 6.5$, respectively. Note that in the frames indicated by (*) the measured quantities depicted in the figures

$(\langle v'_x c' \rangle / U_{max}$ and $\langle v'_x v'_y \rangle / U_{max}^2$ at $z/D_j = 6.5$, respectively) are multiplied by a factor of 2 to spread the false colour scale to account for the lower fluctuations of the frames indicated by (*) compared to the other ones within the same row. The flow conditions were the same as those of Fig. 5.
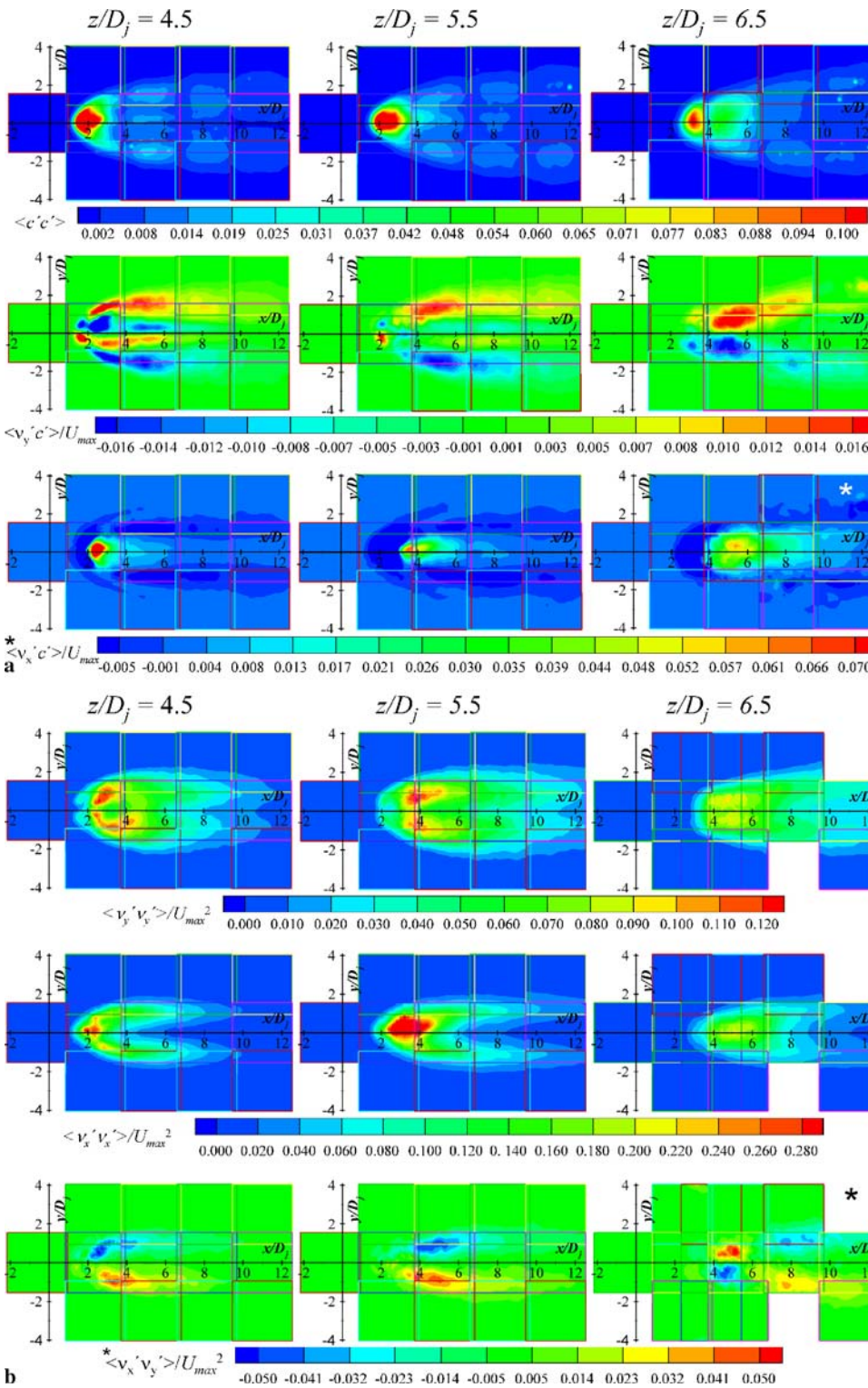
FIGURE 6 (**a**) Two-dimensional maps of measured variances $\langle c'c'\rangle := \overline{c'^2}$ of normalized NO_2-concentration (*top*), normalized Reynolds-fluxes $\langle v'_y c'\rangle/U_{\max}$ (*in the middle*), $\langle v'_x c'\rangle/U_{\max}$ (*bottom*) for various (xy)-planes. Left column represents the (xy)-plane at $z/D_j = 4.5$, the column in the middle the (xy)-plane at $z/D_j = 5.5$ and the right column the (xy)-plane at $z/D_j = 6.5$, respectively. In the frames indicated by (*) the measured quantities are multiplied by a factor of 2. For the flow conditions see Fig. 5. (**b**) Two-dimensional maps of measured Reynolds-stresses $\langle v'_y v'_y\rangle/U^2_{\max}$ (*top*), $\langle v'_x v'_x\rangle/U^2_{\max}$ (*in the middle*) and $\langle v'_x v'_y\rangle/U^2_{\max}$ (*bottom*) for various (xy)-planes. The left column represents the (xy)-plane at $z/D_j = 4.5$, the column in the middle the (xy)-plane at $z/D_j = 5.5$ and the right column the (xy)-plane at $z/D_j = 6.5$, respectively. In the frames indicated by (*) the measured quantities are multiplied by a factor of 2. For flow conditions see Fig. 5

The physical quantities depicted in both figures reflect the enhanced fluxes of a turbulent flow compared to a laminar one caused by the fluctuations of the turbulent flow. Therefore, they are of special concern for the development and validation of models describing turbulent flows. In RANS (Reynolds-averaged Navier-Stokes) as well as for the subgrid scale structures in LES these turbulence quantities have to be described by appropriate models for the Reynolds-stresses, one popular

example being e.g. the k-ε-model developed by Launder and Spalding [30].

From Fig. 6a and b it becomes obvious that the fluctuations in the x-direction exceed the corresponding quantity in the y-direction: $\langle v'_x c'\rangle/U_{\max} > \langle v'_y c'\rangle/U_{\max}$ and $\langle v'_x v'_x\rangle/U^2_{\max} > \langle v'_y v'_y\rangle/U^2_{\max}$. Additionally, it attracts attention that the fluctuations in the relative velocity is significantly larger than those of the relative concentrations $\langle v'_x v'_x\rangle/U^2_{\max} \gg \langle c'c'\rangle$. De-

viations in the magnitude of the (absolute) values of the individual quantities with respect to the (xz)-symmetry-plane of the flow are caused by the "imperfectness" of the flow, the measuring error and an insufficient number of repetitive measurements – the latter is discussed at the end of Sect. 2.2. But, as it can be seen from the false color scale especially e.g. $\langle v'_y c' \rangle / U_{max}$, one has to take into account that a change of the color is carried out in steps of only 0.2%. Therefore, these deviations from the symmetry are comparably small and are emphasized by (the scale of) the false color representation.

It is evident that the interaction between the jet and the crossflow is driven by the jet and the axial velocity component of the crossflow. The jet represents an obstacle for the crossflow on which the latter impinges. Therefore, the highest degree of fluctuation is expected for $\langle c'c' \rangle$, $\langle v'_x v'_x \rangle / U^2_{max}$ and $\langle v'_x c' \rangle / U_{max}$ in the vicinity of the center of the jet trajectory. In these zones, where the highest fluctuations are observed, an intense mixing between the jet and the crossflow is also taking place.

As can be seen from Fig. 6a and b, the location where the jet trajectory intersects the measuring (xy)-plane and where the largest fluctuations are observed is shifted downstream at higher heights above the base plate because the jet is twisted by the momentum of the crossflow. Furthermore, the maximum fluctuations in the normalized concentration are less

twisted than the maximum fluctuations of the axial velocity. This effect can clearly be seen in Fig. 6a and b: e.g. for $z/D_j \approx 6.5$ the maximum fluctuation in the normalized concentration map $\langle c'c' \rangle$ appears at $x/D_j \approx 3.3$ whereas the maximum of $\langle v'_x v'_x \rangle / U^2_{max}$ is found at $z/D_j \approx 5.1$.

A significant velocity-component in the y-direction appears, when the crossflow circulates around the jet which can be regarded as an obstacle. Therefore, it is evident that significant fluctuations of the flow in the y-direction $\langle v'_y v'_y \rangle / U^2_{max}$ can only appear in the shear layer of the jet and the crossflow. As a consequence, especially at lower heights above the base plate zones of high fluctuations appear in a shell like structure around the jet. This structure is favorably formed on the upstream-side of the jet with respect to the crossflow.

Because of the similarity of the structures $\langle c'c' \rangle$ and $\langle v'_x v'_x \rangle / U^2_{max}$ it is not surprising that the structures $\langle v'_y c' \rangle / U_{max}$ and $\langle v'_x v'_y \rangle / U^2_{max}$ look also to some extent quite similar. The fluctuations of the corresponding structures above and below the symmetry-plane have evidently the same magnitude but differ in the sign, because v_y changes the orientation at the symmetry-plane. The structures observed in these frames are possibly caused by the counter-rotating vortex pair depicted in Figs. 3 and 5. At $z/D_j = 4.5$ the v_y-velocity fluctuations in the upper half of the symmetry-plane is in the outer jet shear-layer positively correlated[2] with the fluctuations of the
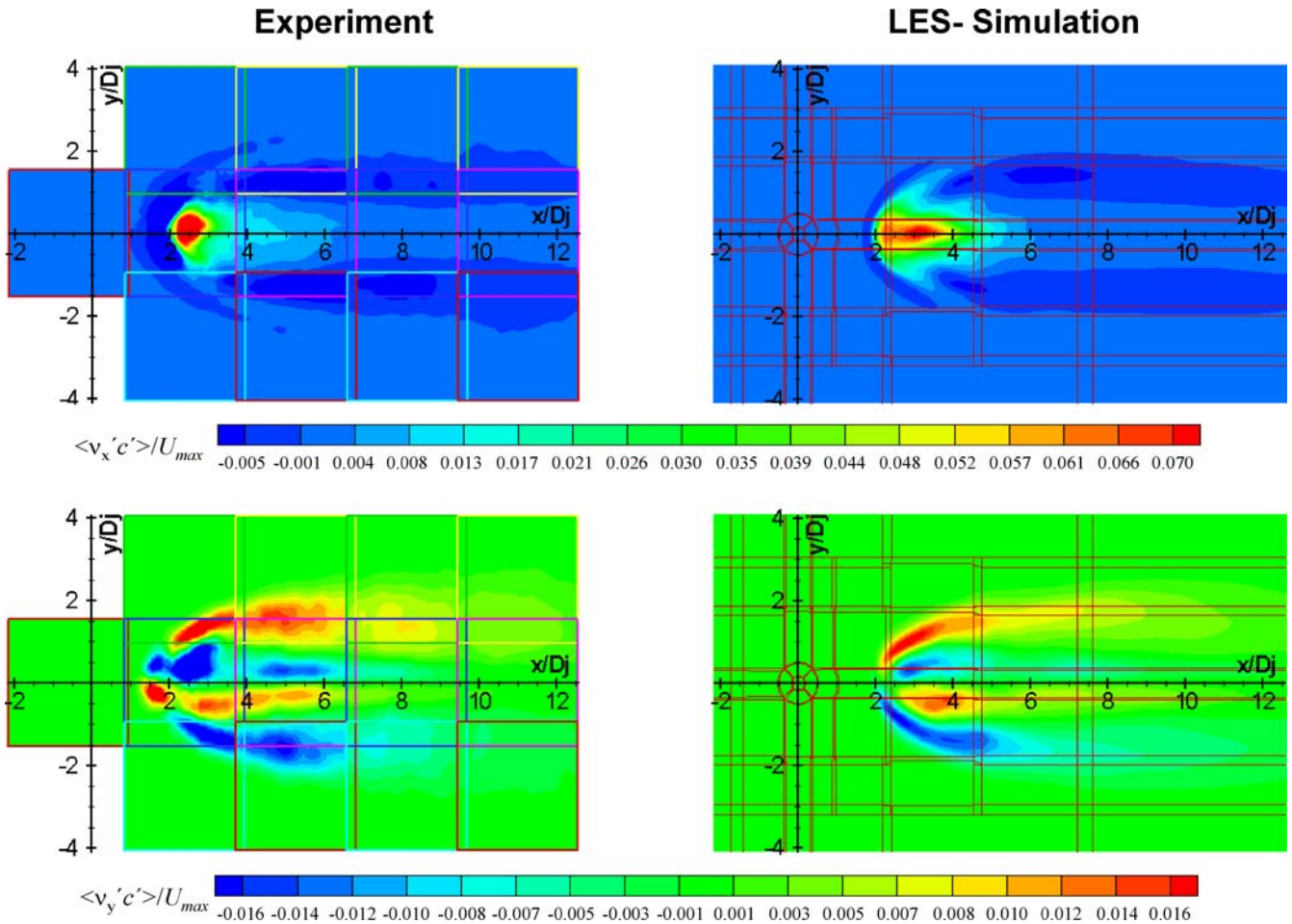

FIGURE 7   Comparison of the experimental results for $\langle v'_x c' \rangle / U_{max}$ and $\langle v'_y c' \rangle / U_{max}$ discussed in Fig. 6a at $z/D_j = 4.5$ with corresponding LES-simulation

concentration, i.e. if v_y increases above the mean value c also rises above its average value and vice versa: if v_y increases above the mean-value more NO$_2$ is transported in the outer region of the structure depicted in the figure. Since in this case v_y and v_y' are > 0, respectively, this would lead to a more or less large (positive) value for the Reynolds-flux. In the lower half with respect to the symmetry-plane a corresponding increase in v_y above the mean value leads to a larger (negative) value whereas the concentration increases like in the upper half with respect to symmetry-plane leading to a large negative value for the flux. The inner structures originate from the recirculating (inner) part of the counter-rotating vortex pair. Therefore, the direction of v_y changes within one and the same half with respect to the symmetry-plane. Consequently, the sign of the structures also changes compared to the outer structures within the same half with respect to the symmetry-plane. As can be seen from Fig. 3 at higher heights above the base-plate, only the structures of the outer jet shear layer appear in Fig. 6a and b. At higher heights the jet is twisted by the crossflow to such an extent, that the recirculating inner shear-layer is underneath the measuring plane. Additionally, these outer structures above and below the symmetry-plane are moving towards each other in the figure, because the measuring plane cuts the jet at its "neck" and not parallel to the total cross-section area of the jet (see Fig. 3). As a further consequence, the separation between the structures visualized in the figures increases in the flow direction (x-direction).

Future experimental and numerical work will be carried out to investigate more deeply the origin of these structures and if also Kelvin–Helmholtz instability [6, 12] contributes to the distribution of these structures. These instabilities lead to a roll up of the jet into a periodic array of ring-like vortices, which leads to increased turbulent fluctuations and macroscale-mixing in the outer shear layer of the jet.

In Fig. 7 the experimental results for $\langle v_x' c' \rangle / U_{\max}$ and $\langle v_y' c' \rangle / U_{\max}$, discussed in Fig. 6a at $z/D_j = 4.5$, are compared with the corresponding LES-simulation, respectively. Having in mind that a change of the color is carried out in steps of only 0.2% for the latter quantity, the agreement between the experiment and the LES is relatively good for the relatively complex shape of $\langle v_y' c' \rangle / U_{\max}$. At this height above the base-plate the widespread structure results from the increased mixing at both inner (close to $y = 0$) and outer (in this figure at approx. $y = \pm 2$) mixing regions of the counter-rotating vortex pair.

4 Conclusions

A Jet-in-Crossflow-arrangement has been built to investigate mixing processes. For this purpose two-dimensional LIF-PIV-measurements have been carried out in order to estimate velocity- as well as scalar concentration-fields in the JCF-arrangement simultaneously. Besides two-

dimensional maps of the mean values of the velocity and the scalar, also quantities which reflect the fluctuation of the flow like variances, turbulence-intensities and especially Reynolds-fluxes and -stresses are estimated quantitatively at various heights above the base-plate of the flow-channel. The latter quantities reflect the enhanced fluxes of a turbulent flow compared to a laminar one. Therefore, they are of special interest with respect to the investigation of turbulence phenomena and mixing processes and for the development and validation of models for the Reynolds-fluxes and -stresses.

In both flows (the jet and the crossflow) droplets were added for PIV-measurement. Additionally, NO$_2$ is added to the jet as a molecular tracer for the LIF-measurements. NO$_2$ is chosen as the tracer, because it absorbs the wavelength of the frequency doubled Nd:YAG-laser used for the PIV-measurements. Consequently, one single laser in combination with two cameras is used to measure the quantities just mentioned.

The experimental results were compared with LES-simulations of the flow. Taking into account the complexity of the structures and the smallness of the maximum relative value of the fluctuations (e.g. for $\langle v_y' c' \rangle / U_{\max} < 2\%$) and the change in the color code that happens for very small differences ($\langle v_y' c' \rangle / U_{\max} : 0.2\%$), there is a good agreement between the experimental results and the numerical simulation.

From these investigations it seems that the counter-rotating vortex pair has a significant influence on the magnitude of the fluctuating quantities and consequently on the mixing behavior of both flows. Further investigations will be carried out in a future work in order to investigate this finding in more detail and to estimate the influence of the different vortex-structures of a JCF onto these quantities as well.

5 List of symbols

$\langle c \rangle$:	normalized time-averaged concentration $(C/C_{\mathrm{jet}})\,[-]$
$[C]$:	concentration [mol/l]
f:	focal length [mm]
k:	contraction ratio of the square nozzle of the crossflow $[-]$
n:	number of images
Q:	volume based flowrate, [m$_n^3$/h]
r:	momentum-flux ratio $(\varrho_j U_j^2 / \varrho_\infty U_\infty^2)^{1/2}$ equal to the bulk velocity ratio (U_j/U_∞) for constant density $[-]$
$R(\phi_1, \phi_2)$:	one point correlation function $[-]$
$R_{\max}$@532 nm:	reflectivity [%]
$T_{\max}$:	transmission [%]
Tu:	turbulence intensity (Tu $= \sigma/\phi_{\mathrm{mean}} \times 100$) [%]
Tu$_x$:	turbulence intensity along x-axis (Tu$_x = \sigma(v_x)/\langle v_x \rangle \times 100$) [%]
U:	bulk velocity (Q/Area) [m/s]
$\boldsymbol{v}$:	velocity vector with time-averaged components $\langle v_x \rangle$, $\langle v_y \rangle$, $\langle v_z \rangle$ [m/s]
$\langle v_x' c' \rangle$:	time-averaged Reynolds-fluxes, [m/s]
$\langle v_x' v_x' \rangle$:	time-averaged Reynolds-stresses [m^2/s^2]
$\langle c' c' \rangle$, (or $\overline{c'^2}$):	time-averaged variance of the normalized scalar concentration $[-]$

---

[2] Point correlation coefficients $R(\phi_1, \phi_2)$ between two physical quantities are defined by $R(\phi_1, \phi_2) = \dfrac{\overline{\phi_1' \cdot \phi_2'}}{\sqrt{\overline{\phi_1'^2}}\sqrt{\overline{\phi_2'^2}}}$. Because the denominator serves for scaling-reasons ($-1 \leq R(\phi_1, \phi_2) \leq +1$), the Reynolds-fluxes e.g. $\langle v_y' c' \rangle / U_{\max}$ can be interpreted as "differently scaled" correlation coefficients.

U_{max}:   maximum axial velocity over the total cross-section area [m/s]

Greek symbols

ϱ: density of the gas [kg/m³]

σ: standard deviation

σ_{mean}: $(\sigma/n^{1/2})$

ϕ_{mean}:   mean value (obtained by averaging of n images) of the velocity or the concentration

Subscripts

j: jet

x, y, z: axis of the coordinate system

∞:   crossflow

Superscripts

′:   fluctuating quantity: $\phi' = \phi_{instant} - \phi_{mean} = \phi_{instant} - \langle\phi\rangle$

REFERENCES

1 R.J. Margason, *Fifty years of jet in crossflow research*, In: *AGARD Symp. On a Jet in Cross Flow* (Winchester, UK, AGARD CP-534, 1993)

2 J.F. Keffer, W.D. Baines, J. Fluid. Mechan. **15**, 481 (1963)

3 Y. Kamotani, I. Greber, AIAA J. **10**, 11 (1972)

4 J. Andreopoulos, W. Rodi, J. Fluid. Mech. **138**, 93 (1984)

5 E.F. Hasselbrink, M.G. Mungal, J. Fluid. Mech. **443**, 1 (2001)

6 R.M. Kelso, T.T. Lim, A.E. Perry, J. Fluid. Mech. **306**, 111 (1996)

7 R. Camussi, G. Guj, A. Stella, J. Fluid. Mech. **454**, 113 (2002)

8 M.W. Plesniak, D.M. Cusano, J. Fluid. Mech. **524**, 1 (2005)

9 S.H. Smith, M.G. Mungal, J. Fluid. Mech. **357**, 83 (1998)

10 T.F. Fric, A. Roshko, J. Fluid. Mech. **279**, 1 (1994)

11 S.L.V. Coelho, J.C.R. Hunt, J. Fluid. Mech. **200**, 95 (1989)

12 L.L. Yuan, R.L. Street, J.H. Ferziger, J. Fluid. Mech. **379**, 71 (1999)

13 L.K. Su, M.G. Mungal, J. Fluid. Mech. **513**, 1 (2004)

14 R.J. Adrian, Exp. Fluids **39**, 159 (2005)

15 C.E. Niederhaus, F.H. Champagne, J.W. Jacobs, AIAA J. **11**, 1697 (1997)

16 J.E. Rehm, N.T. Clemens, AIAA Paper No. 97-0250 (1997)

17 E.F. Hasselbrink, M.G. Mungal, R.K. Hanson, AIAA Paper No. 97-0118 (1997)

18 C.D. Carter, J.M. Donbar, J.F. Driscoll, Appl. Phys. B **66**, 129 (1998)

19 L.K. Su, M.G. Mungal, Ann. Res. Briefs 19 (1999)

20 E.F. Hasselbrink, M.G. Mungal, J. Fluid. Mech. **443**, 27 (2001)

21 R.J. Cattolica, *Combustion-torch Ignition: Fluorescence Imaging of NO₂*, 21st Symp. (Int.) on Combustion (The Combustion Inst., Pittsburgh, 1551, 1986)

22 D. Most, A. Leipertz, Appl. Opt. **40**, 5379 (2001)

23 D. Most, F. Dinkelacker, A. Leipertz, *Direct Detection of the Turbulent Flux by Simultaneous Application of Filtered Rayleigh-Scattering Thermometry and Particle Image Velocimetry*, 29st Symp. (Int.) on Combustion (The Combustion Inst., Pittsburgh, 2669, 2002)

24 O. Özcan, K.E. Meyer, P.S. Larsen, C.H. Westergaard, *Simultaneous measurements of Velocity and Concentration in a Jet in Channel-Crossflow* (Proc. FEDSM, ASME Fluids Eng. Div. Summer Meeting, New Orleans, USA, 2001)

25 L. Prandtl, *Führer durch die Strömungslehre* (Vieweg, Braunschweig, 1990)

26 G.-G. Böger, *Optimierung von Windkanaldüsen für den Unterschallbereich*, Dissertation, Ruhr-Universität Bochum (1973)

27 M. Raffel, C.E. Willert, J. Kompenhans, *Particle Image Velocimetry – A Practical Guide* (Springer, Berlin, 1998)

28 A. Gulati, R.E. Warren, J. Propul. Power **1**, 54 (1994)

29 M. García-Villalba, J. Fröhlich, W. Rodi, Phys. Fluids **18**, 55 (2006)

30 B.E. Launder, D.B. Spalding, *Lectures in Mathematical Models of Turbulence* (Academic Press, New York, 1972)